Complex Pattern Formation from Current-Driven Dynamics of Single-Layer Homoepitaxial Islands on Crystalline Conducting Substrates

Ashish Kumar, Dwaipayan Dasgupta, and Dimitrios Maroudas*

Department of Chemical Engineering, University of Massachusetts Amherst, Amherst, Massachusetts 01003-9303, USA

(Received 19 April 2017; revised manuscript received 16 June 2017; published 27 July 2017)

We report a systematic study of complex pattern formation resulting from the driven dynamics of single-layer homoepitaxial islands on surfaces of face-centered-cubic (fcc) crystalline conducting substrates under the action of an externally applied electric field. The analysis is based on an experimentally validated nonlinear model of mass transport via island edge atomic diffusion, which also accounts for edge diffusional anisotropy. We analyze the morphological stability and simulate the field-driven evolution of rounded islands for an electric field oriented along the fast edge diffusion direction. For larger-than-critical island sizes on {110} and {100} fcc substrates, we show that multiple necking instabilities generate complex island patterns, including not-simply-connected void-containing islands mediated by sequences of breakup and coalescence events and distributed symmetrically with respect to the electric field direction. We analyze the dependence of the formed patterns on the original island size and on the duration of application of the external field. Starting from a single large rounded island, we characterize the evolution of the number of daughter islands and their average size and uniformity. The evolution of the average island size follows a universal power-law scaling relation, and the evolution of the total edge length of the islands in the complex pattern follows Kolmogorov-Johnson-Mehl-Avrami kinetics. Our study makes a strong case for the use of electric fields, as precisely controlled macroscopic forcing, toward surface patterning involving complex nanoscale features.

DOI: 10.1103/PhysRevApplied.8.014035

I. INTRODUCTION

Generating nanoscale patterns on surfaces by directing the motion of clusters of atoms through precise control of the action of externally applied macroscopic forces constitutes an essential enabling tool in the field of nanofabrication. Toward this end, obtaining a comprehensive fundamental understanding of the dynamics of surface features driven by such externally applied macroscopic forcing is of great significance. It has been demonstrated that the collective motion of atoms adsorbed on crystalline substrate surfaces can be driven in a controlled manner by electric fields or thermal gradients through the transport phenomena of electromigration [1–9] or thermomigration [10,11]. In general, the ability to drive mass transport on surfaces through the use of macroscopic forces has been demonstrated at both mesoscopic and nanoscopic length scales in various material systems ranging from metal conductors [2] to colloids [12] and block copolymers [13–15] to liquid droplets [16].

Among such macroscopic-force-driven assembly processes, the phenomena of electromigration-driven assembly of crystalline conducting surface features such as single-layer islands and voids have been studied extensively through both atomistic simulation and continuum-domain simulation studies [7–9,17,18]. Theoretical studies have identified various mechanisms of mass transport [19–22], with atomic transport through periphery or edge diffusion being the dominant of these diffusional transport processes. An important experimental study [2] based on *in situ* scanning tunneling microscopy has shown that such homoepitaxial islands on metallic substrates move in the direction of electron flow through edge atomic diffusion with a migration speed that is inversely proportional to the island size, d_0 (where $d_0 = 2 \times \sqrt{\text{island area}/\pi}$). Starting from a single monolayer-thick island with a shape merely perturbed from being perfectly rounded [23], a previous study of current-driven single-layer island dynamics on crystalline conducting substrates [17] has reported that the electric field, in conjunction with edge diffusional anisotropy, triggers a morphological instability on the edge of the migrating islands, with size d_0 greater than a critical island size d_c resulting in formation of features such as protrusions, fingers, and narrow necks on the island's edge. Islands on face-centered-cubic (fcc) substrate surfaces that are larger than the critical size d_c have been shown to undergo a so-called necking instability, which leads to the breakup of the parent island into an assembly of daughter islands resulting in pattern formation on the substrate surface [24–26]; such patterns include arrays of nanowires with confined widths [25] and assemblies of small uniformly sized islands arranged in linear or V-shaped arrays [26].

*maroudas@ecs.umass.edu

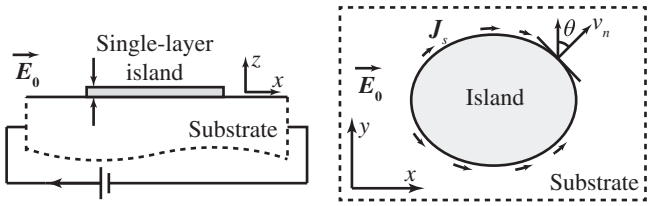

FIG. 1. Schematic representation of a single-layer epitaxial island with a rounded edge morphology on a crystalline conducting substrate under the action of an electric field. The x-y plane of a Cartesian frame of reference corresponds to the substrate surface plane.

In this article, we study the dynamics of single-layer homoepitaxial rounded islands with an initial size d_0 that is larger than the critical size d_c on surfaces of fcc substrates under the action of an externally applied electric field that is oriented along the fast edge diffusion direction. In our notation, island size refers to the island-equivalent diameter (i.e., a length equal to the diameter of a circular island that has the same area as the actual island). Islands on $\{110\}$ and $\{100\}$ fcc substrate surfaces with $d_0 > d_c$ undergo necking, which results in the breakup of the parent island into daughter islands that continue to migrate in the direction of the electric field and may undergo coalescence or further breakup depending upon their size, speed, and instantaneous morphology. Starting from a single island with a rounded morphology, as shown in Fig. 1, these sequences of breakup and coalescence events result in the formation of an entire population of daughter islands in a pattern that is complex, symmetric with respect to the applied electric field direction, and increasingly distributed far from the symmetry axis with time. We show that this complex evolving pattern can be frozen in place on the substrate surface by switching off the electric field. Without the action of the electric field, the islands attain their equilibrium morphology. The evolution of patterns under the action of the electric field also leads to formation of islands that are nonsimply connected, containing one or more voids. These non-simply-connected void-containing islands, upon switching the electric field off, result in formation of stable void-containing islands. The simplest of these islands resemble nanoring structures [27,28], which are known for their optical and plasmonic properties [29,30] and constitute very promising nanostructures for the fabrication of optoelectronic [31,32], sensing [33], and magnetic data-storage devices [34–36]. The nanorings formed in our study have single-layer height and lateral sizes on the order of 10 nm. Further, we characterize in detail the evolution of the island population by monitoring the number of daughter islands, the total edge length (sum of the perimeters of all islands in the island population) in the island pattern, the average size of the daughter islands in an evolving island population, and the island size uniformity in the island population. We find that the evolution of the total edge length follows Kolmogorov-Johnson-Mehl-Avrami kinetics [37–39] and that the evolution of the average island area follows a universal scaling law. Eventually, the current-driven island dynamics reaches a steady state. Moreover, upon turning off the electric field, the individual daughter islands achieve their equilibrium morphology resulting in a complex stable, frozen-in nanopattern. We characterize the nanopatterns and show that as the duration of the electric field action increases, the mean island diameter of the resulting island population in the pattern converges toward the critical island size d_c required for necking for the given fcc substrate surface. The distribution of island sizes in a population also becomes more uniform with time.

II. MODEL AND METHODS

The initial configuration of an epitaxial monolayer-thick rounded island is shown in Fig. 1 on the crystalline solid substrate surface that corresponds to the x-y plane of a Cartesian frame of reference. The current-driven evolution of this rounded island is monitored by time stepping the continuity equation, according to which the normal velocity v_n at any point on the island edge is proportional to the edge divergence of the mass flux along the island edge J_s. The dominant mode of mass transport in such single-layer islands is edge diffusion [19–21], consistent with the findings of the experimental study of Ref. [2]. Terrace diffusion and evaporation-condensation kinetics are neglected for the size of the metallic islands and the temperature range considered in this study (several tens of degrees above room temperature) [2,19–21]. The applied electric field that drives island electromigration [1–9] is aligned with the Cartesian x axis and has strength E_0. The flux J_s is expressed by a Nernst-Einstein equation [7,17] resulting in the continuity equation

$$v_n = -\Omega \frac{\partial}{\partial s}\left\{\frac{D_s(\theta,\varepsilon_m)}{k_B T}\left[-\frac{\partial \mu}{\partial s} + q_s^* E_s\right]\right\}. \qquad (1)$$

In Eq. (1), Ω is the atomic area, s is the arc length along the island's edge, $D_s(\theta,\varepsilon_m) = D_{s,\max}(\varepsilon_m) f(\theta)$ is the edge atomic diffusivity where θ is the edge orientation (Fig. 1), $f(\theta)$ is the diffusional anisotropy function, ε_m is the misfit strain ($\varepsilon_m = 0$ and $\varepsilon_m \neq 0$ for homoepitaxial and heteroepitaxial islands, respectively), k_B is the Boltzmann constant, T is temperature, $\mu = (\tilde{\gamma} + \tilde{\gamma}_{\rm el})\Omega\kappa$ is the chemical potential of an edge atom with the edge stiffness $\tilde{\gamma}$ taken to be isotropic [7,17], $\tilde{\gamma}_{\rm el}$ is the elastic contribution to the island edge tension [17], $\kappa = d\theta/ds$ is the local edge curvature, q_s^* is the effective charge of an atom at the island edge, and $q_s^* E_s$ is the local component of the electromigration force, tangent to the island's edge, as typically expressed in all phenomenological models of driven atomic transport due to electromigration [1–4,6,7]. It should be emphasized that elastic effects are absent in homoepitaxial islands ($\varepsilon_m = 0$ and $\tilde{\gamma}_{\rm el} = 0$) and that isotropic edge stiffness implies a rounded

island morphology at equilibrium. The local approximation $E_s = E_0 \cos\theta$ [7] is justified by the 2D nature of the single-layer islands, which renders nonlocal effects, such as current crowding, negligible. From the dimensional analysis of Eq. (1), we derive the characteristic length scale l_E as $l_E = \sqrt{\tilde{\gamma}\Omega/|q_s^* E_0|}$ and the characteristic time scale τ as $\tau = l_E^4/[D_{s,\max}\tilde{\gamma}\Omega^2/(k_B T)]$. We mention that we use notation that is standard in the island electromigration modeling literature [7,17]: l_E is the proper dynamic length scale for the driven edge atomic transport problem, from balancing edge stiffness with the edge electromigration force, and Ω is directly related to the atomic volume in the single-layer island taking the edge thickness (interlayer distance) into account. From the physical parameters reported in Ref. [2], we determine l_E and τ to be 13.6 nm and 32.5 s, respectively.

The dependence of D_s on ε_m is discussed in Ref. [17]. For fcc crystalline substrate surfaces, the edge diffusional anisotropy $D_s(\theta) = D_{s,\max} f(\theta)$ is accounted for by using a three-parameter anisotropy function $f(\theta) = \{1 + A\cos^2[m(\theta+\phi)]\}/(1+A) \leq 1$; $A > 0$ is the anisotropy strength, ϕ is the misorientation angle formed by the direction of the externally applied field and the fast edge diffusion direction, and m is the number of fast edge diffusion directions determined by the surface crystallographic orientation. This integer parameter m provides the continuum evolution model Eq. (1) with some atomistic information for the substrate surface structure; $m = 1$, 2, and 3 correspond to $\{110\}$, $\{100\}$, and $\{111\}$ substrate surfaces, respectively [7,17]. Surface reconstructions, which may be common over a broader class of materials, will complicate $f(\theta)$ and require proper modification of its present functional form. We have validated the above model by comparing its predictions for the stable driven island morphologies and the island migration speed dependence on the island size with the experimental data of Ref. [2] ([17]).

We use direct dynamical simulations to explore the dynamics of large-size homoepitaxial rounded islands ($d_0 > d_c$), such as that shown schematically in Fig. 1, to identify what patterns emerge when the electric field is oriented along the fast edge diffusion direction ($\phi = 0$) and to understand how to control and design these patterns. The key parameters that we vary in this simulation study are the initial island size d_0, the substrate surface orientation m, and the duration for which the electric field is applied t_a before it is turned off. In all our simulations, $\phi = 0$, and the electric field is aligned with the positive x axis. The simulation methodology for time stepping, front tracking, and handling of island breakup and coalescence processes is identical to that described in Ref. [24].

III. RESULTS AND DISCUSSION

Under the action of an electric field oriented along the fast edge diffusion direction, on $\{110\}$ and $\{100\}$ substrate surfaces, the islands that have sizes greater than the critical size d_c undergo necking and break up into daughter islands [17]. If the daughter islands formed as a result of this necking instability have sizes smaller than the critical island size d_c, they migrate in the direction of the electric field with a stable morphology at a constant speed [17].

From our simulations, we determine the critical island size required for triggering the necking instability d_c to be $3.7 l_E$ and $8.2 l_E$ for $\{110\}$ and $\{100\}$ substrate surfaces, respectively. These critical island sizes are computed following systematic numerical protocols, such as that in Ref. [17]. They mark the computed onset of necking undergone by the island's edge and are expressed in units of l_E. For the range of island sizes that we examine in our study, the islands migrating on $\{111\}$ substrate surfaces ($m = 3$) under the action of the electric field do not undergo necking and breakup to form daughter islands. Instead, on $\{111\}$ substrate surfaces, islands undergo a fingering transition, which leads to the formation of a protrusion at the island's leading edge. Eventually, under the action of the electric field, the islands' evolution on these substrates ($m = 3$) transitions to their migrating at an angle with the electric field direction with a more stable faceted morphology, as is reported in Ref. [17].

Figures 2(a1)–2(a6) show a representative sequence of configurations during the current-driven evolution of a near-rounded single-layer island on a $\{110\}$ fcc substrate surface ($m = 1$); in Fig. 2, t denotes the time elapsed since the electric field was turned on. On large islands under the action of the electromigration force, edge morphological instabilities cause the formation of protrusions at multiple locations along the island's edge. The number of locations where such protrusions appear increases with increasing initial island size d_0. The locations of these protrusions on the island edge are arranged symmetrically with respect to the direction of the externally applied electric field. The protrusions grow to form narrow necks, and the edge evolves further leading to the breakup of the initial island into daughter islands. The daughter islands with sizes greater than the critical size for necking d_c undergo further necking instabilities and breakup. Because smaller islands migrate faster than larger ones, smaller-sized daughter islands produced at or near the trailing end in an evolving pattern may catch up, depending on their exact location and pattern features, with the larger daughter islands located ahead of them in the pattern near or at its leading end. If a trailing smaller island is on a collision course with a larger island ahead of it, the two islands will coalesce giving rise to a larger island. Such a sequence of breakup and coalescence events may lead to the formation of non-simply-connected void-containing islands. This is because, during coalescence, the trailing island and the leading island may trap some void space between them generating a vacancy island (void) within the larger postcoalescence island. Voids can also be generated if a neck forms on a

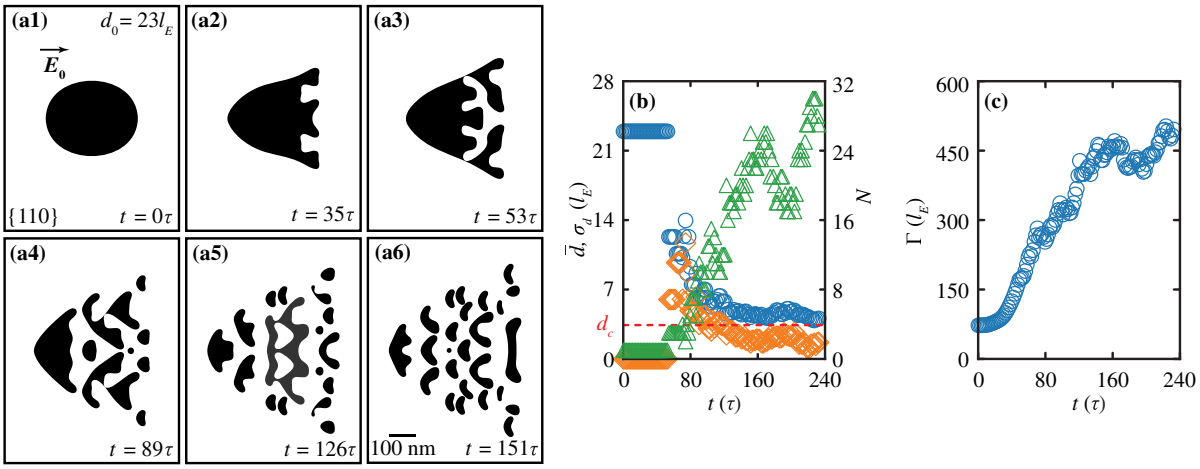

FIG. 2. (a1)–(a6) Sequences of configurations generated from the current-driven evolution of the island shown in (a1) on a {110} fcc substrate surface. The electric field is oriented along the fast edge diffusion direction and is aligned with the x axis. (b) Evolution of the mean island diameter of the population of islands $\bar{d}$ (blue open circles), the standard deviation of the island diameter of the population, σ_d (orange open diamonds), and the number of islands in the island population, N (green open triangles) in the dynamical pattern formed under the action of the electric field. The red dashed line represents the critical island size d_c required for necking on {110} fcc substrate surfaces. (c) Evolution of the total edge length (sum of the perimeters) of all the islands in the island population Γ (blue open circles) in the dynamical pattern formed on the {110} fcc substrate surface under the action of the electric field. Parameter values: $m = 1$, $\phi = 0$, $d_0 = 23l_E$.

sufficiently large island leading to a formation of a horseshoelike edge morphological feature. The ends of the horseshoe-shaped island after breakup may come in contact with each other, thus, trapping void space within this island. In such non-simply-connected islands, voids migrate due to edge atomic diffusional transport in the direction opposite to that of the islands' migration.

In the evolving complex island patterns, as the number of islands N increases due to the breakup processes with the increasing duration of application of the electric field, the average island size $\bar{d}$ in the resulting island population decreases and becomes increasingly more uniform; the island size distribution tends toward a steady state characterized by an average island size equal to that required for necking d_c, which is marked by the horizontal dashed red line in Fig. 2(b). Together with the evolution of $\bar{d}$, Fig. 2(b) also shows the evolution of the standard deviation of the island size of the population σ_d and the number of islands in the population of the pattern N; it is evident that σ_d converges to 0 as $\bar{d}$ converges to d_c. After the first set of breakup events, the subsequent breakup and coalescence events happen at a fast rate because of the presence of a large number of necks in the islands of the pattern and of a larger number of islands in the pattern in close proximity to each other on the substrate surface. The steady state reached by the island size is understood because no further breakup can occur after the islands reach the critical size of d_c and since islands of the same size migrate at the same speed, therefore, avoiding collisions leading to coalescence. Figure 2(c) shows the evolution of the total edge length of the pattern, i.e., the sum of the perimeters of all the islands in the population Γ. Turning off the electric field at any given point in time causes the individual islands in the population to stop migrating and attain their equilibrium (rounded) morphologies due to curvature-driven edge diffusion, resulting in a stable equilibrium pattern of static islands. For example, upon turning off the electric field, the evolving patterns shown in Figs. 2(a5) and 2(a6) reach the stable equilibrium patterns of Figs. 4(g2) and 4(g4), respectively. During such a pattern equilibration, islands that are in close proximity to each other may coalesce as they evolve toward their equilibrium-rounded morphology due to the rearrangement of the individual islands' edges.

For all initial island sizes, we examine the evolution of the average island area of an island population resulting from the breakup of the initial larger-than-critical island. Figure 3(a) shows the plot of the dimensionless average island area $\tilde{A}$ as a function of dimensionless time $\tilde{t}$, where the dimensionless quantities are defined as

$$\tilde{A} = \frac{\bar{A} - A_c}{A_0 - A_c} \tag{2}$$

and

$$\tilde{t} = \frac{t - t_n}{\tau}. \tag{3}$$

In Eq. (2), $\bar{A}$ is the average area of the islands in the population in the evolving nanopattern, A_c is the critical (minimum) island area required for a necking instability (and, hence, breakup of the parent island into daughter

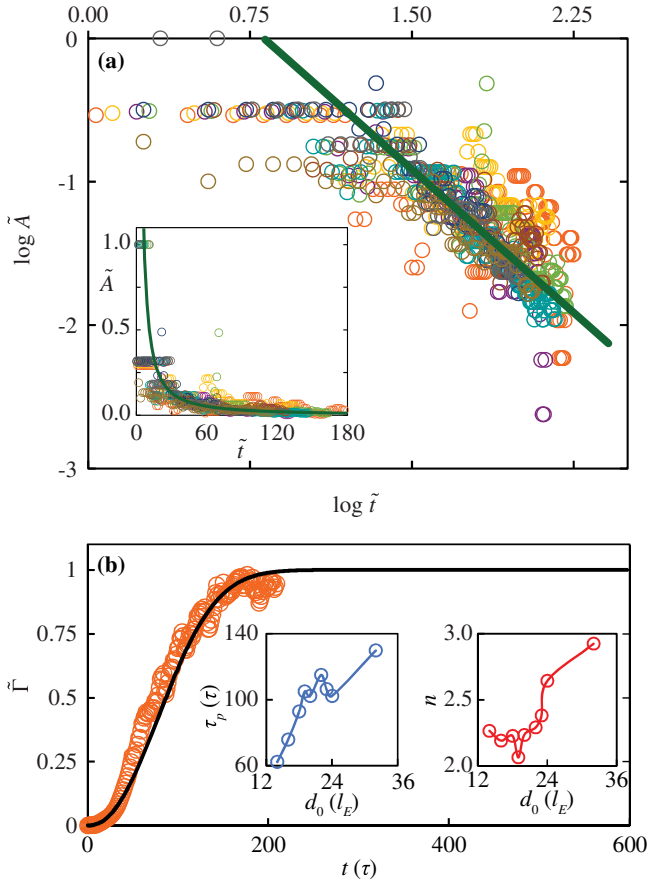

FIG. 3. (a) Logarithmic (log-log) plot of the evolution of the average dimensionless area $\tilde{A}$ of the islands forming in an evolving complex pattern on a {110} fcc substrate surface as a function of dimensionless time $\tilde{t}$. The normal plot of the evolution of $\tilde{A}$ as a function of $\tilde{t}$ is shown in the inset. The variously colored open circles correspond to data for the current-driven evolution of larger-than-critical islands on {110} fcc substrate surfaces ($m = 1$) with initial island sizes of $d_0 = 14l_E$, $d_0 = 16l_E$, $d_0 = 18l_E$, $d_0 = 19l_E$, $d_0 = 20l_E$, $d_0 = 22l_E$, $d_0 = 23l_E$, $d_0 = 24l_E$, and $d_0 = 32l_E$. In both plots, the solid lines correspond to the best fit of the data according to the scaling relation $\tilde{A} \sim \tilde{t}^{-1.3304}$. (b) Representative plot of the evolution of the dimensionless total edge length of all the islands in the pattern $\tilde{\Gamma}$ (orange open circles) as a function of t on a {110} fcc substrate surface for an initial island size $d_0 = 20l_E$. The black solid line corresponds to the best fit of the data according to Eq. (5). The two insets show the dependence of the relaxation time τ_p and the exponent n in Eq. (5) on d_0.

islands) to occur, and A_0 is the area of the initial island. In Eq. (3), t is a given time instant in the simulation, with the electric field turned on at $t = 0$, t_n is the time of occurrence of the first set of breakup events for a given initial island size, and τ is the characteristic diffusional time scale. The evolution of $\tilde{A}$ reaches eventually a steady state characterized by an average island area of the island population in the pattern equal to the critical island area required for necking A_c. The linear long-time scaling shown by the straight-line fit of the data in the log-log plot of the evolution of $\tilde{A}$ in Fig. 3(a) implies that, at long times, the evolution of $\tilde{A}$ follows a power law with an exponent α: for {110} fcc substrate surfaces, the corresponding scaling relation is $\tilde{A} \sim \tilde{t}^{-1.3304\pm0.0312}$, i.e., $\alpha \approx -4/3$. The reported statistical error corresponds to a 90% confidence interval in the slope calculation over the range of d_0 values examined in the analysis. Since $\tilde{A} = C\tilde{t}^{\alpha}$, where C is a constant, the number of islands in the evolving pattern can be estimated as a function of time as $N = A_0/\tilde{A}$, i.e.,

$$N = \frac{A_0}{A_0 C\tilde{t}^{\alpha} + A_c(1 - C\tilde{t}^{\alpha})}. \tag{4}$$

In the long-time limit, the number of islands obtained is $N_{\tilde{t}\to\infty} = A_0/A_c$, as expected from the convergence of the island size to its steady-state value discussed above and shown in Fig. 2(b).

Under the constant application of the electric field, the total edge length Γ for all initially larger-than-critical island sizes grows over time as shown in Fig. 3(b) for a representative case with $d_0 = 20l_E$. Analysis of the simulation results throughout the parameter space explored in this study shows that the evolution of the dimensionless total edge length $\tilde{\Gamma}$ can be described on the basis of Kolmogorov-Johnson-Mehl-Avrami kinetics [37–39] involving a compressed exponential function of t,

$$\tilde{\Gamma} = \frac{\Gamma - \Gamma_0}{\Gamma_{t\to\infty} - \Gamma_0} = 1 - \exp\left[\left(-\frac{t}{\tau_p}\right)^n\right]. \tag{5}$$

In Eq. (5), Γ_0 is the perimeter (edge length) at $t = 0$ of the original rounded island that undergoes breakup under the action of the external field giving rise to the island population of the pattern, $\Gamma_{t\to\infty}$ is the total edge length of a population of daughter islands of uniform size equal to the critical island size d_c required for necking, τ_p is the corresponding relaxation time, and the exponent $n > 1$. The solid line in Fig. 3(b) shows the least-squares fit of the data according to Eq. (5). The relaxation time τ_p and the exponent n obtained from the best fit of the simulation data are plotted as functions of the initial island size d_0 in the insets in Fig. 3(b). τ_p increases almost monotonically with increasing d_0, which can be understood qualitatively on the basis of atomic transport through edge diffusion that requires longer time for larger-sized islands. The exponent n lies between 2.0 and 3.0 and also exhibits almost monotonic increase with increasing d_0.

Figure 4 shows various representative final stable patterns obtained for various initial island sizes as a function of the duration for which the electric field is applied, t_a, before it is switched off. After the electric field is turned off, each island in the population is let to achieve its equilibrium-rounded morphology. The final stable patterns obtained are

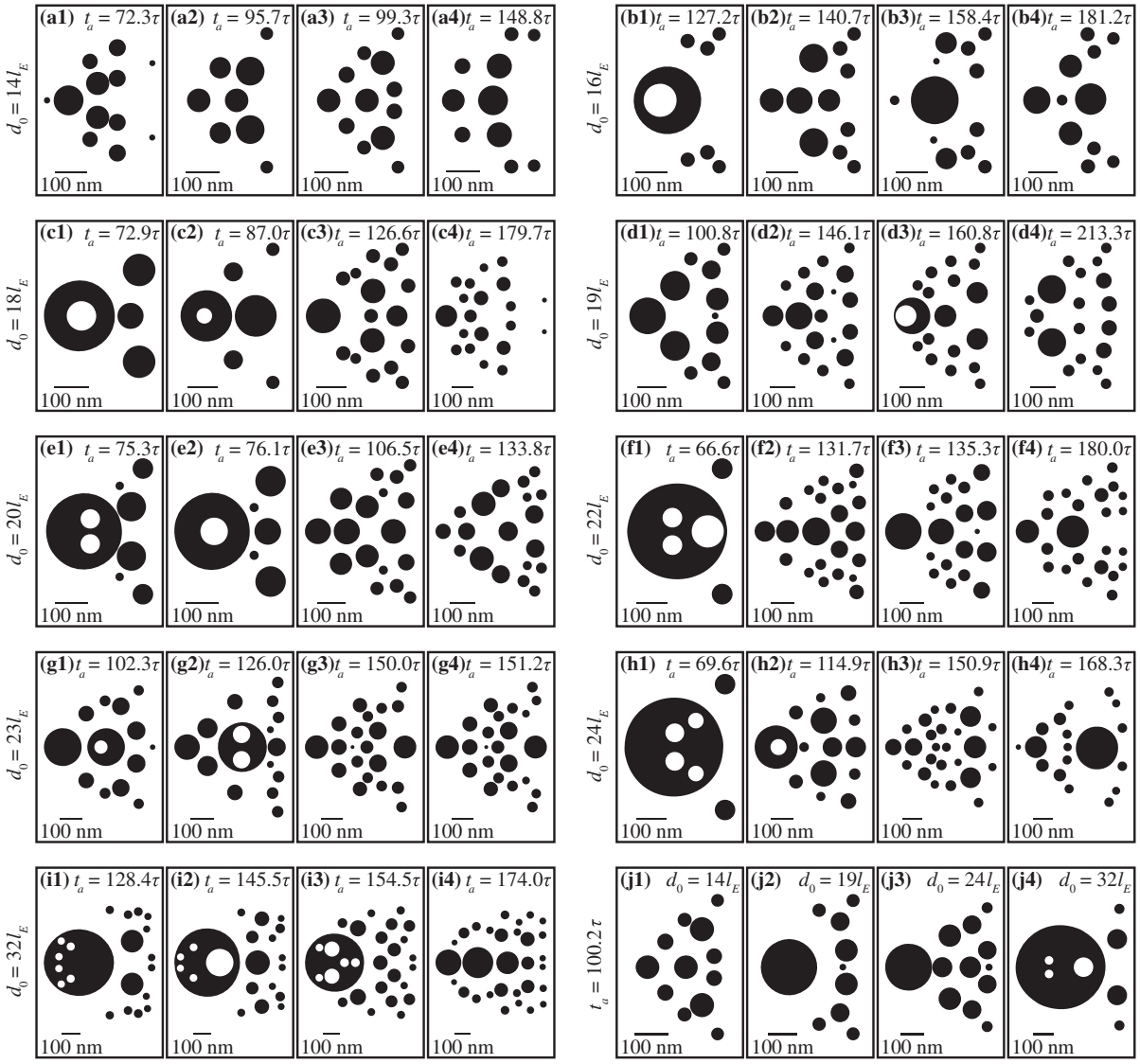

FIG. 4. Representative sequences of equilibrium configurations consisting of complex patterns formed on $\{110\}$ fcc substrate surfaces ($m = 1$) from the current-driven evolution of larger-than-critical single-layer rounded islands after the electric field, which was oriented along the fast edge diffusion direction ($\phi = 0$), aligned with the x axis, and applied for a time period t_a has been turned off, and the islands of the resulting patterns are let to equilibrate and obtain their equilibrium-rounded morphology. The initial island size is (a1)–(a4) $d_0 = 14l_E$, (b1)–(b4) $d_0 = 16l_E$, (c1)–(c4) $d_0 = 18l_E$, (d1)–(d4) $d_0 = 19l_E$, (e1)–(e4) $d_0 = 20l_E$, (f1)–(f4) $d_0 = 22l_E$, (g1)–(g4) $d_0 = 23l_E$, (h1)–(h4) $d_0 = 24l_E$, and (i1)–(i4) $d_0 = 32l_E$. (j) Sequences of equilibrium configurations of island patterns at a fixed $t_a = 100.2\tau$ for increasing, from (j1) to (j4), initial island size d_0.

fairly complex, and their complexity increases with increasing initial island size d_0 and duration of application of the external field t_a. The equilibrium patterns formed on $\{110\}$ substrate surfaces are symmetric with respect to an axis aligned with the direction of the applied electric field. With increasing t_a, the number of daughter islands in the final stable pattern increases, and the islands get distributed increasingly farther from the pattern's symmetry axis. The non-simply-connected domains (islands containing voids) that are generated as the pattern evolves may lead to formation of stable non-simply-connected islands in the final stable patterns as shown, for example, in Figs. 4(b1), 4(c1), and 4(c2). In the absence of external forcing, these non-simply-connected domains also achieve their stable equilibrium annular, ringlike morphology due to curvature-driven edge diffusion. The islands on the left of the equilibrium patterns of Figs. 4(b1), 4(c1), 4(c2), and 4(e2), i.e., some of the simplest of the void-containing islands in the patterns of Fig. 4, constitute the smallest possible nanoring structures because of their single-layer thickness. It is worth noting that these nanorings are not generated because of lattice mismatch or thermal mismatch in a strained deposited film [28] but due to the action of an electric field on unstrained homoepitaxial islands. It should

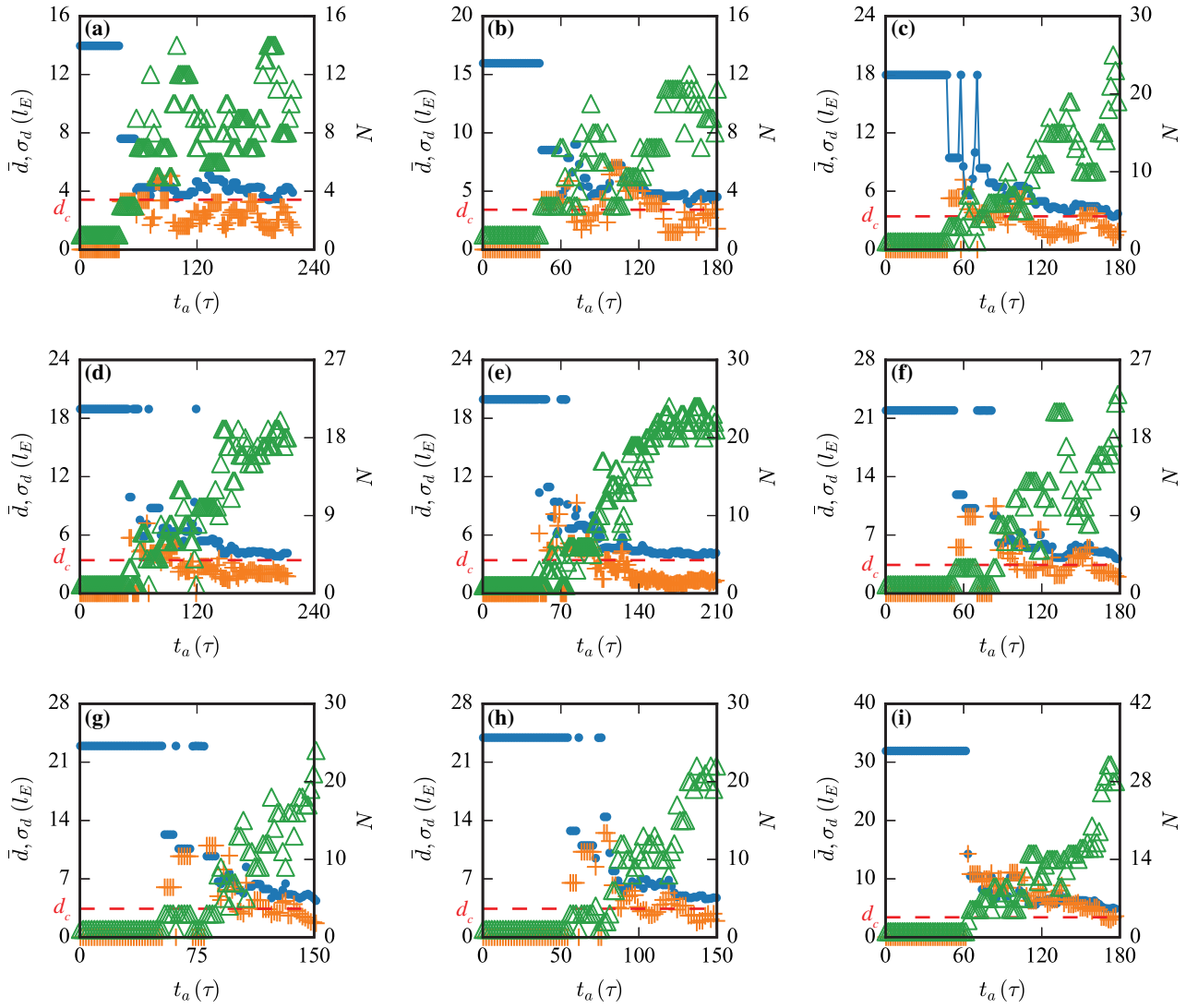

FIG. 5. Characterization of complex patterns formed from current-driven dynamics of larger-than-critical single-layer epitaxial islands on {110} surfaces of fcc crystalline conducting substrates: Mean island diameter of a population of islands $\bar{d}$ (blue solid circles), standard deviation of the diameters of the islands in a population σ_d (orange crosses), and number of islands in the island population N (green open triangles) of a given complex pattern as a function of the duration of application of the electric field t_a before it is turned off for an initial island size of (a) $d_0 = 14l_E$, (b) $d_0 = 16l_E$, (c) $d_0 = 18l_E$, (d) $d_0 = 19l_E$, (e) $d_0 = 20l_E$, (f) $d_0 = 22l_E$, (g) $d_0 = 23l_E$, (h) $d_0 = 24l_E$, and (i) $d_0 = 32l_E$. When applied, the electric field is oriented along the fast edge diffusion direction ($\phi = 0$) and aligned with the x axis. After the electric field is turned off, the resulting patterns are let to equilibrate until each island obtains its equilibrium-rounded morphology. The red dashed line represents the critical island size d_c required for necking on {110} fcc substrate surfaces.

also be mentioned that stabilizing such nanoring configurations requires careful control of t_a, since non-simply-connected domains cannot be stabilized at long times, i.e., in the long-t_a limit, the island pattern contains only simply connected island domains as is evident in Fig. 4; note the absence of void-containing islands in the equilibrium patterns of Figs. 4(a4), 4(b4), 4(c4), 4(d4), 4(e4), 4(f4), 4(g4), 4(h4), and 4(i4). For completeness, Fig. 4(j) shows sequences of equilibrium configurations of island patterns at a fixed value of the duration of electric field application $t_a = 100.2\tau$ for increasing, from Fig. 4(j1) to 4(j4), initial island size d_0 in order to clarify the diversity exhibited by these equilibrium island patterns at given t_a over the range of initial island sizes examined.

We characterize these complex equilibrium patterns on {110} substrates as a function of the duration of the applied electric field in Fig. 5; $t_a = 0$ in the plots of Fig. 5 implies that the electric field is never turned on. Figure 5 shows the mean island size of the population of islands in the equilibrium pattern $\bar{d}$, the standard deviation of the island sizes of the population σ_d, and the number of islands N in the equilibrated pattern as functions of t_a for various initial island sizes. The general trends of N, $\bar{d}$, and σ_d with increasing t_a in the equilibrium patterns follow those of the

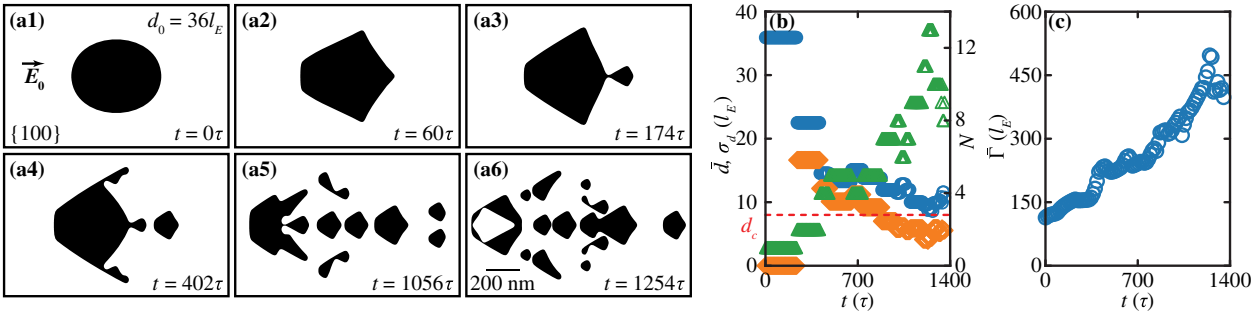

FIG. 6. (a1)–(a6) Sequences of configurations generated from the current-driven evolution of the island shown in (a1) on a {100} fcc substrate surface. The electric field is oriented along the fast edge diffusion direction and is aligned with the x axis. (b) Evolution of the mean island diameter of the population of islands $\bar{d}$ (blue open circles), the standard deviation of the island diameter of the population σ_d (orange open diamonds), and the number of islands in the island population N (green open triangles) in the dynamical pattern formed under the action of the electric field. The red dashed line represents the critical island size d_c required for necking on {100} fcc substrate surfaces. (c) Evolution of the total edge length (sum of the perimeters) of all the islands in the island population Γ (blue open circles) in the dynamical pattern formed on the {100} fcc substrate surface under the action of the electric field. Parameter values: $m = 2, \phi = 0, d_0 = 36l_E$.

evolution of N, $\bar{d}$, and σ_d under the action of the external field shown in the case of Fig. 2(b). Therefore, with increasing t_a, the average island size of the population of islands in the equilibrium pattern converges to the critical island size required for necking d_c; this critical island size is indicated by the horizontal dashed red lines in all the plots of Fig. 5. As a result, the size distribution of the islands in the equilibrium pattern becomes more uniform with increasing t_a, leading to a convergence toward a value of zero of its standard deviation σ_d in the long-t_a limit.

The current-driven dynamics of single-layer islands observed on {100} substrate surfaces ($m = 2$) is similar to the complex dynamics observed on {110} substrate surfaces ($m = 1$). The two main differences observed in the island dynamics on {100} surfaces compared to that on {110} surfaces are that the driven island evolution on {100} substrate surfaces leads to formation of distinct edge facets which are not seen on {110} substrates and that, depending upon the formation process of the daughter islands after necking, the daughter islands migrate either in the direction of the electric field or at an angle with the field direction. Facets seen on the migrating islands' edge on {100} substrate surfaces are not observed on islands migrating on {110} substrate surfaces because such edge facet formation is observed only for substrate surfaces with symmetry higher than threefold, expressed by an anisotropy parameter $m \geq 1.5$ [7]. Figures 6(a1)–6(a6) show a representative case for the current-driven dynamics of a larger-than-critical sized island on a {100} substrate surface. Starting from a rounded morphology, such a large island on a {100} substrate surface first undergoes a fingering instability. The fingering instability is followed by the formation of a narrow neck, Fig. 6(a3), and the breaking up from the parent island of a daughter island formed from the leading tip of the finger following a necking instability. This kind of necking and breakup generates a daughter island that migrates in the direction of the electric field. Breakup of the parent island on a {100} substrate surface also can happen through fingering and necking near the vertices of the island in symmetric locations from its leading end, Fig. 6(a4), that generates daughter islands which migrate at an angle with the field direction and have faceted morphologies that feature a standing wave on one of the island sides resembling the edge features near the necks in the "side wings" of the island in Fig. 6(a4). Islands in the resultant evolving pattern undergo a sequence of breakup and coalescence events similar to those occurring in evolving patterns on {110} substrates surfaces. Such patterns on {100} substrates also feature non-simply-connected void-containing islands similar to those forming in the evolving patterns on {110} substrate surfaces. Figure 6(b) shows the evolution of the mean island size of the population of islands in the evolving pattern $\bar{d}$, the standard deviation of the island size of the population σ_d, and the number of islands N in the island population of the pattern formed from the current-driven evolution of the large rounded island of Fig. 6(a1). Eventually, the evolution of $\bar{d}$ and σ_d converges to their steady-state values of d_c and zero, respectively. Figure 6(c) depicts the evolution of the total edge length of the islands in the pattern Γ. The time required for the resulting island pattern to approach a steady state on {100} surfaces is close to 1 order of magnitude longer than that on {110} substrate surfaces due to the slower island migration velocities on surfaces of higher (crystallographic) symmetry m of edge diffusional anisotropy [17]; such slower migration speeds imply longer times between island coalescence events.

Figure 7(a) shows the evolution of the dimensionless average area $\tilde{A}$ for a range of initial island sizes $22l_E \leq d_0 \leq 38l_E$ on {100} substrates. Following the same statistical analysis conducted for the data sets of Fig. 3(a) shows that the dimensionless average area evolves

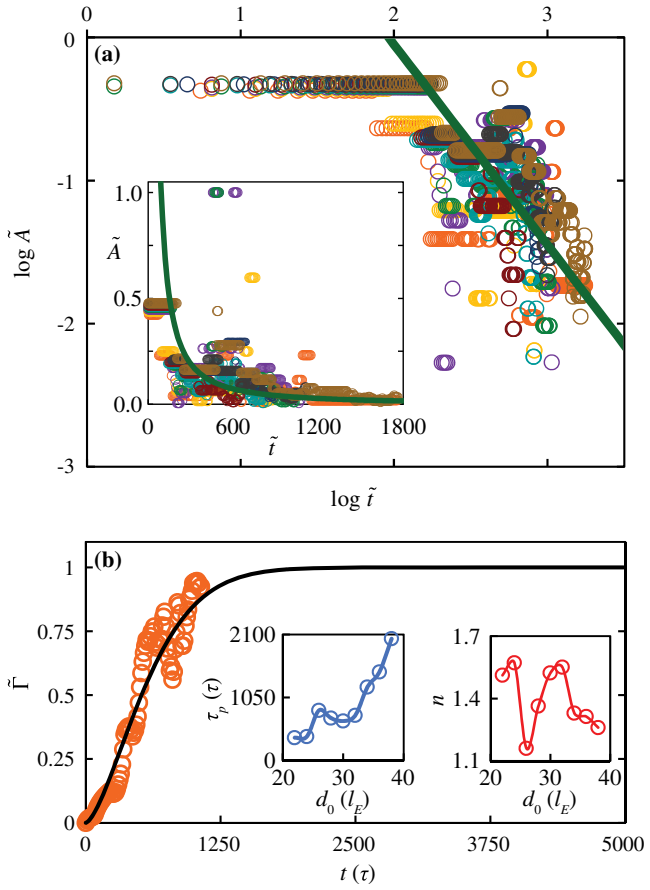

FIG. 7. (a) Logarithmic (log-log) plot of the evolution of the average dimensionless area $\tilde{A}$ of the islands forming in an evolving complex pattern on a {100} fcc substrate surface as a function of dimensionless time $\tilde{t}$. The normal plot of the evolution of $\tilde{A}$ as a function of $\tilde{t}$ is shown in the inset. The variously colored open circles correspond to data for the current-driven evolution of larger-than-critical islands on {100} fcc substrate surfaces ($m = 2$) with initial island sizes of $d_0 = 22l_E$, $d_0 = 24l_E$, $d_0 = 26l_E$, $d_0 = 28l_E$, $d_0 = 30l_E$, $d_0 = 32l_E$, $d_0 = 34l_E$, $d_0 = 36l_E$, and $d_0 = 38l_E$. In both plots, the solid lines correspond to the best fit of the data according to the scaling relation $\tilde{A} \sim \tilde{t}^{-1.4118}$. (b) Representative plot of the evolution of the dimensionless total edge length of all the islands in the pattern $\tilde{\Gamma}$ (orange open circles) as a function of t on a {100} fcc substrate surface for an initial island size $d_0 = 30l_E$. The black solid line corresponds to the best fit of the data according to Eq. (5). The two insets show the dependence of the relaxation time τ_p and the exponent n in Eq. (5) on d_0.

according to the scaling relation $\tilde{A} \sim \tilde{t}^{-1.4118\pm0.0873}$, i.e., a power law that is universal throughout the range of d_0 examined, with an exponent close to that of the respective power law on {110} surfaces, $\alpha = -1.4118 \approx -4/3$. The straight-line fit in the log-log plot of Fig. 7(a) confirms the power-law behavior at long times and gives the exponent α as a fitting parameter. Figure 7(b) shows the evolution under constant electric field action of the dimensionless total edge length $\tilde{\Gamma}$, for a representative case with $d_0 = 30l_E$. Consistent with the Avrami kinetics on {110} surfaces, the evolution of $\tilde{\Gamma}$ follows the relationship of Eq. (5) on {100} substrate surfaces too. The dependence of the relaxation time τ_p and the exponent n in Eq. (5) on the initial island size d_0 is plotted in the insets in Fig. 7(b); both τ_p and n are obtained as fitting parameters by fitting the simulation data according to Eq. (5) as shown in Fig. 7(b). For the current-driven island dynamics on {100} substrate surfaces, τ_p again increases almost monotonically with increasing d_0, while n lies in the range $1.1 \leq n \leq 1.6$ and fluctuates around a mean value of approximately 1.4.

The Avrami kinetics, Eq. (5), followed by the growth of the total edge length of the islands in the current-driven patterns that form both on {110} and {100} substrate surfaces when the electric field direction is aligned with the fast edge diffusion direction is an important result for nanopattern design and engineering on conducting substrate surfaces. A rigorous derivation of Eq. (5) and prediction of the compressed exponential function parameters τ_p and n requires further theoretical analysis of the island dynamics, i.e., analysis based on a coarse-grained description of island migration [17], coalescence, and breakup that mediate the island pattern formation. Such a theoretical analysis is beyond the scope of this study and will be pursued elsewhere. Of course, the fundamental dynamics that governs all of these processes is that of edge atomic diffusion and electromigration-induced drift, as described by Eq. (1) and the accompanying relations for the edge atomic chemical potential and diffusivity required for its closure.

Figures 8(a)–8(i) show representative equilibrium patterns obtained on {100} substrates as a function of the duration of application of the electric field t_a for various initial island sizes d_0; sequences of equilibrium island patterns at $t_a = 802\tau$ over the range of initial island sizes d_0 examined are shown in Fig. 8(j). The stable patterns obtained on {100} substrate surfaces are similar to those obtained on {110} substrate surfaces. The equilibrium shape of the islands in the final equilibrated patterns is rounded because in our model the edge stiffness γ is considered to be isotropic. The facets observed during the current-driven evolution of the islands are due to a kinetic anisotropy (edge diffusional anisotropy), and, hence, they do not feature in the final stable pattern. Because of the higher critical island diameter for necking d_c on {100} than on {110} substrate surfaces, the number of islands obtained in the equilibrium pattern on {100} substrate surfaces is smaller than that on {110} surfaces for the same initial island size. The final stable (equilibrium) patterns obtained on {100} surfaces are complex, and, consistent, with the patterns on {110} surfaces, their complexity increases with increasing initial island size d_0 and duration of application of the external field t_a. Each equilibrium pattern in Fig. 8 is symmetric with respect

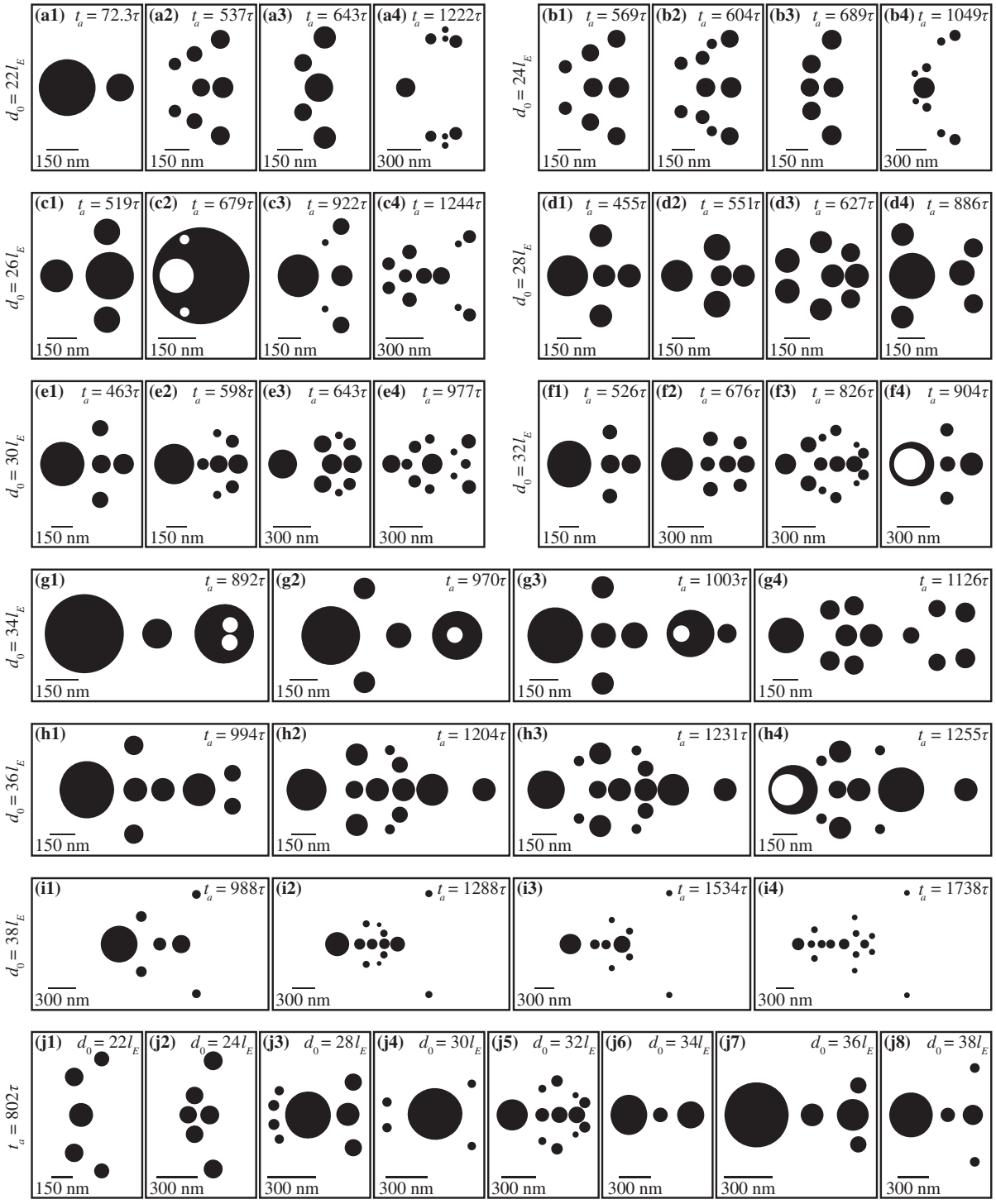

FIG. 8. Representative sequences of equilibrium configurations consisting of complex patterns formed on $\{100\}$ fcc substrate surfaces ($m = 2$) from the current-driven evolution of larger-than-critical single-layer rounded islands after the electric field, which was oriented along the fast edge diffusion direction ($\phi = 0$), aligned with the x axis, and applied for a time period t_a has been turned off, and the islands are let to equilibrate and obtain their equilibrium-rounded morphology. The initial island size is (a1)–(a4) $d_0 = 22l_E$, (b1)–(b4) $d_0 = 24l_E$, (c1)–(c4) $d_0 = 26l_E$, (d1)–(d4) $d_0 = 28l_E$, (e1)–(e4) $d_0 = 30l_E$, (f1)–(f4) $d_0 = 32l_E$, (g1)–(g4) $d_0 = 34l_E$, (h1)–(h4) $d_0 = 36l_E$, and (i1)–(i4) $d_0 = 3l_E$. (j) Sequences of equilibrium configurations of island patterns at a fixed $t_a = 802\tau$ for increasing, from (j1) to (j8), initial island size d_0.

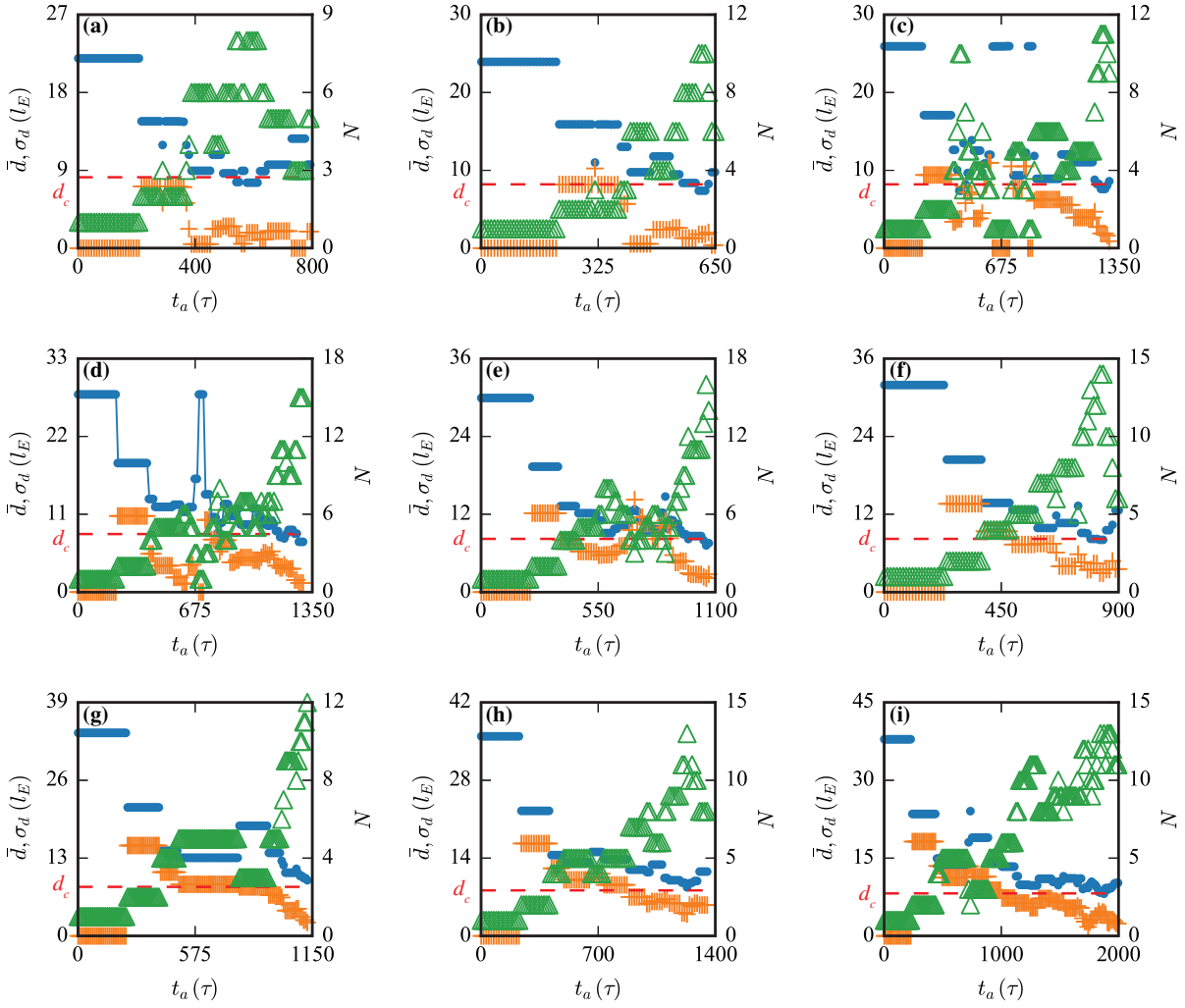

FIG. 9. Characterization of complex patterns formed from current-driven dynamics of larger-than-critical single-layer epitaxial islands on {100} surfaces of fcc crystalline conducting substrates: Mean island diameter of a population of islands $\bar{d}$ (blue solid circles), standard deviation of the diameters of the islands in a population in a given complex pattern σ_d (orange crosses), and number of islands in the island population N (green open triangles) of a given complex pattern as a function of the duration of application of the electric field t_a before it is turned off for an initial island size of (a) $d_0 = 22l_E$, (b) $d_0 = 24l_E$, (c) $d_0 = 26l_E$, (d) $d_0 = 28l_E$, (e) $d_0 = 30l_E$, (f) $d_0 = 32l_E$, (g) $d_0 = 34l_E$, (h) $d_0 = 36l_E$, and (i) $d_0 = 38l_E$. When applied, the electric field is oriented along the fast edge diffusion direction ($\phi = 0$) and aligned with the x axis. After the electric field is turned off, the resulting patterns are let to equilibrate until each island obtains its equilibrium-rounded morphology. The red dashed line represents the critical island size d_c required for necking on {100} fcc substrate surfaces.

to an axis aligned with the electric field direction, and, with increasing t_a, the daughter islands are distributed increasingly farther from the symmetry axis. It should be mentioned that in the equilibrium island patterns of Figs. 4 and 8, the total island area A (shaded area in these figures) remains constant and equal to the area of the original rounded island $A = A_0 = \pi {d_0}^2/4$, which guarantees mass conservation during both current-driven evolution and subsequent equilibration upon switching off the external field. Although individual islands in the patterns may grow (due to coalescence) or shrink (due to breakup), the total island area of each pattern, which is equal to the sum of the areas of all the islands in the pattern, is conserved. We check thoroughly in all of our simulations and confirm that total island area conservation is satisfied; this is guaranteed by the accuracy and precision of our numerical integration of the continuity equation, Eq. (1).

Finally, Fig. 9 shows the characterization of the complex equilibrium patterns on {100} surfaces as a function of the duration of the applied electric field t_a. All of the trends observed in the patterns on these substrate surfaces with $m = 2$ in the long-t_a limit are consistent with those observed in the characterization of the equilibrium patterns obtained on substrate surfaces with $m = 1$. We further mention that the trends shown in Figs. 5 and 9 may give the impression that the plotted quantities are multivalued

functions of t_a. This is clearly not the case: this false impression may be created due to the large fluctuations in the variation of the plotted quantities with t_a during the initial stages of the evolution process as a result of island breakup and coalescence events during the equilibration period after the field is switched off. To clarify this feature in the data sets, we connect the mean island diameter $\bar{d}(t_a)$ data points in Figs. 5(c) and 9(d) with solid lines.

For the range of island sizes examined in this study, the current-driven islands migrating on {111} substrate surfaces ($m = 3$) do not break up to form patterns consisting of populations of daughter islands. Islands on {111} surfaces undergo a fingering transition which leads to the formation of a protrusion at the island's leading edge. The corresponding island morphology is similar to that shown in Fig. 6(a2). However, this type of morphology is unstable on {111} substrate surfaces, and the migrating islands transform to a stable faceted morphology and begin migrating at an angle with the electric field direction. Before the migrating island's shape transitions to a stable faceted morphology, the edge diffusional dynamics leads to the formation of necks similar to that shown in Fig. 6(a3), but the edge of the islands remain intact, i.e., no breakup is triggered, and, therefore, there is no formation of daughter islands accompanying the current-driven dynamics of large islands on {111} substrate surfaces. Instead, islands with faceted edge shapes exhibit oscillatory dynamics on {111} surfaces and are characterized by a morphology with a stable straight edge on one side of the island and a standing edge wave on the other side, while the island migrates at constant speed in the direction of the straight edge. Detailed characterization and analysis of such complex oscillatory dynamics are beyond the scope of the present article and will be discussed elsewhere.

IV. SUMMARY AND CONCLUSIONS

In summary, we demonstrate that morphological instabilities on the edge of a larger-than-critical single-layer island migrating on {110} or {100} surfaces of fcc crystalline substrates under the action of an electric field that is oriented along the fast edge diffusion direction can lead to the formation of intriguingly complex patterns consisting of assemblies of single-layer islands smaller than the original island and arranged symmetrically with respect to the electric field direction. We characterize in detail the evolving complex patterns of the island assemblies, with the initial island size and the duration of application of the electric field being the key pattern formation parameters. We show that the evolution of the average area of the islands in the assembly under the action of the electric field follows a universal kinetic relation and that the evolution of the total edge length of the formed assembly of islands, for all initial island sizes examined, follows Avrami kinetics. We also characterize the stable patterns formed after the electric field is turned off, and we show that the average island size and the uniformity of an island population in a complex pattern, for all initial island sizes, reach a steady state as the duration of application of the electric field increases. These stable complex patterns upon switching off the electric field feature formation of the smallest observed nanorings with single-layer height and lateral sizes on the order of tens of nanometers, a range of length scales that is barely accessible through the use of e-beam lithography. Therefore, we describe a current-induced approach for the formation of metallic nanoring structures, which have very appealing properties toward applications in optoelectronics and data storage systems: starting from an array of deposited epitaxial islands, electric fields can be used to create arrays of such fine nanorings by exploiting electromigration-driven morphological dynamics, which allows for formation of unique geometries and selection of nanometer-scale sizes.

In closing, we mention that we expect the current-driven dynamics of coherently strained single-layer heteroepitaxial islands on crystalline conducting substrates to be qualitatively similar to that of the homoepitaxial islands analyzed in this study, leading to analogously complex pattern formation mediated by island breakup and coalescence processes. Specifically, as reported in Ref. [17], the current-driven single-layer heteroepitaxial islands exhibit a similar linear dependence of island migration speed on the inverse of the island size at small island sizes, as well as a critical island size d_c beyond which the rounded island edge becomes unstable; however, for heteroepitaxial islands, the critical island sizes are greater than those for homoepitaxial islands [17]. Moreover, misfit strain has a direct effect on the atomic mobility for edge diffusion and, thus, affects significantly the island migration speed [40,41]: specifically, tensile misfit strain leads to a decrease in the island migration speed, while compressive misfit strain accelerates the translational motion of the island [17]. Therefore, depending on whether the misfit strain is tensile or compressive, the island coalescence rate will be slower or faster, respectively, which will affect quantitatively the island pattern formation kinetics. Such current-driven dynamics of heteroepitaxial islands and the resulting complex pattern formation will be explored in a future publication.

ACKNOWLEDGMENT

This work was supported by the U.S. Department of Energy, Office of Basic Energy Sciences, Division of Materials Sciences and Engineering, under Award No. DE-FG02-07ER46407.

[1] K.-N. Tu, *Solder Joint Technology: Materials, Properties, and Reliability* (Springer, New York, 2007), pp. 211–243.

[2] C. Tao, W. G. Cullen, and E. D. Williams, Visualizing the electron scattering force in nanostructures, Science **328**, 736 (2010).

[3] V. Tomar, M. R. Gungor, and D. Maroudas, Current-Induced Stabilization of Surface Morphology in Stressed Solids, Phys. Rev. Lett. **100**, 036106 (2008).

[4] D. Maroudas, Surface morphological response of crystalline solids to mechanical stresses and electric fields, Surf. Sci. Rep. **66**, 299 (2011).

[5] A. Latz, S. P. Sindermann, L. Brendel, G. Dumpich, F.-J. Meyer zu Heringdorf, and D. E. Wolf, Anisotropy of electromigration-induced void and island drift, J. Phys. Condens. Matter **26**, 055005 (2014); M. Jongmanns, A. Latz, and D. E. Wolf, Impurity-induced island pinning during electromigration, Europhys. Lett. **110**, 16001 (2015).

[6] F. Barakat, K. Martens, and O. Pierre-Louis, Nonlinear Wavelength Selection in Surface Faceting under Electromigration, Phys. Rev. Lett. **109**, 056101 (2012).

[7] P. Kuhn, J. Krug, F. Hausser, and A. Voigt, Complex Shape Evolution of Electromigration-Driven Single-Layer Islands, Phys. Rev. Lett. **94**, 166105 (2005).

[8] P. Kuhn and J. Krug, in *Multiscale Modeling in Epitaxial Growth*, edited by Axel Voigt, ISNM International Series of Numerical Mathematics Vol. 149 (Birkhäuser, Basel, 2005), pp. 159–173.

[9] M. Rusanen, P. Kuhn, and J. Krug, Kinetic Monte Carlo simulations of oscillatory shape evolution for electromigration-driven islands, Phys. Rev. B **74**, 245423 (2006).

[10] K.-N. Tu, *Solder Joint Technology: Materials, Properties, and Reliability* (Springer, New York, 2007), pp. 327–346.

[11] D. Dasgupta, G. I. Sfyris, M. Rauf Gungor, and D. Maroudas, Surface morphological stabilization of stressed crystalline solids by simultaneous action of applied electric and thermal fields, Appl. Phys. Lett. **100**, 141902 (2012); L. Du, D. Dasgupta, and D. Maroudas, Stabilization of the surface morphology of stressed solids using thermal gradients, Appl. Phys. Lett. **104**, 181901 (2014); Stabilization of the surface morphology of stressed solids using simultaneously applied electric fields and thermal gradients, J. Appl. Phys. **116**, 173501 (2014).

[12] R. C. Hayward, D. A. Saville, and I. A. Aksay, Electrophoretic assembly of colloidal crystals with optically tunable micropatterns, Nature (London) **404**, 56 (2000).

[13] C. W. Pester, C. Liedel, M. Ruppel, and A. Böker, Block copolymers in electric fields, Prog. Polym. Sci. **64**, 182 (2017).

[14] E. Schaffer, T. Thurn-Albrecht, T. P. Russell, and U. Steiner, Electrically induced structure formation and pattern transfer, Nature (London) **403**, 874 (2000).

[15] T. L. Morkved, M. Lu, A. M. Urbas, E. E. Ehrichs, H. M. Jaeger, P. Mansky, and T. P. Russell, Local control of microdomain orientation in diblock copolymer thin films with electric fields, Science **273**, 931 (1996).

[16] N. Bjelobrk, H. L. Girard, S. Bengaluru Subramanyam, H.-M. Kwon, D. Quéré, and K. K. Varanasi, Thermocapillary motion on lubricant-impregnated surfaces, Phys. Rev. Fluids **1**, 063902 (2016).

[17] D. Dasgupta, G. I. Sfyris, and D. Maroudas, Current-driven morphological evolution of single-layer epitaxial islands on crystalline substrates, Surf. Sci. **618**, L1 (2013).

[18] J.-J. Metois, J.-C. Heyraud, and A. Pimpinelli, Steady-state motion of silicon islands driven by a dc current, Surf. Sci. **420**, 250 (1999).

[19] O. Pierre-Louis and T. L. Einstein, Electromigration of single-layer clusters, Phys. Rev. B **62**, 13697 (2000).

[20] H. Mehl, O. Biham, O. Millo, and M. Karimi, Electromigration-induced flow of islands and voids on the Cu(001) surface, Phys. Rev. B **61**, 4975 (2000).

[21] S. V. Khare, N. C. Bartelt, and T. L. Einstein, Diffusion of Monolayer Adatom and Vacancy Clusters: Langevin Analysis and Monte Carlo Simulations of their Brownian Motion, Phys. Rev. Lett. **75**, 2148 (1995); S. V. Khare and T. L. Einstein, Brownian motion and shape fluctuations of single-layer adatom and vacancy clusters on surfaces: Theory and simulations, Phys. Rev. B **54**, 11752 (1996); Unified view of step-edge kinetics and fluctuations, Phys. Rev. B **57**, 4782 (1998).

[22] O. U. Uche, D. Perez, A. F. Voter, and J. C. Hamilton, Rapid Diffusion of Magic-Size Islands by Combined Glide and Vacancy Mechanism, Phys. Rev. Lett. **103**, 046101 (2009).

[23] M. Schimschak and J. Krug, Electromigration-Induced Breakup of Two-Dimensional Voids, Phys. Rev. Lett. **80**, 1674 (1998).

[24] D. Dasgupta and D. Maroudas, Surface nanopatterning from current-driven assembly of single-layer epitaxial islands, Appl. Phys. Lett. **103**, 181602 (2013).

[25] A. Kumar, D. Dasgupta, C. Dimitrakopoulos, and D. Maroudas, Current-driven nanowire formation on surfaces of crystalline conducting substrates, Appl. Phys. Lett. **108**, 193109 (2016).

[26] A. Kumar, D. Dasgupta, and D. Maroudas, Surface nanopattern formation due to current-induced homoepitaxial nanowire edge instability, Appl. Phys. Lett. **109**, 113106 (2016).

[27] C. Somaschini, S. Bietti, N. Koguchi, and S. Sanguinetti, Fabrication of multiple concentric nanoring structures, Nano Lett. **9**, 3419 (2009).

[28] F. Ruffino, I. Crupi, F. Simone, and M. G. Grimaldi, Formation and evolution of self-organized Au nanorings on indium-tin-oxide surface, Appl. Phys. Lett. **98**, 023101 (2011).

[29] E. M. Larsson, J. Alegret, M. Käll, and D. S. Sutherland, Sensing characteristics of NIR localized surface plasmon resonances in gold nanorings for application as ultrasensitive biosensors, Nano Lett. **7**, 1256 (2007).

[30] S. Kim, J.-M. Jung, D.-G. Choi, H.-T. Jung, and S.-M. Yang, Patterned arrays of Au rings for localized surface plasmon resonance, Langmuir **22**, 7109 (2006).

[31] M. Shioi, K. Lodewijks, L. Lagae, T. Kawamura, and P. Van Dorpe, Tuning plasmonic interaction between gold nanorings and a gold film for surface enhanced Raman scattering, Appl. Phys. Lett. **97**, 163106 (2010).

[32] X. Fang, Z. Li, Y. Long, H. Wei, R. Liu, J. Ma, M. Kamran, H. Zhao, X. Han, B. Zhao, and X. Qiu, Surface-Plasmon-Polariton Assisted Diffraction in Periodic Subwavelength Holes of Metal Films with Reduced Interplane Coupling, Phys. Rev. Lett. **99**, 066805 (2007).

[33] J. Aizpurua, P. Hanarp, D. S. Sutherland, M. Käll, G. W. Bryant, and F. J. García de Abajo, Optical Properties of Gold Nanorings, Phys. Rev. Lett. **90**, 057401 (2003).

[34] L. W. Yu, K. J. Chen, J. Song, J. Xu, W. Li, X. F. Li, J. M. Wang, and X. F. Huang, New Self-Limiting Assembly Model for Si Quantum Rings on Si(100), Phys. Rev. Lett. **98**, 166102 (2007).

[35] X. F. Han, Z. C. Wen, and H. X. Wei, Nanoring magnetic tunnel junction and its application in magnetic random access memory demo devices with spin-polarized current switching (invited), J. Appl. Phys. **103**, 07E933 (2008).

[36] Z. C. Wen, H. X. Wei, and X. F. Han, Patterned nanoring magnetic tunnel junctions, Appl. Phys. Lett. **91**, 122511 (2007).

[37] A. Nikolaevich Kolmogorov, On the statistical theory of the crystallization of metals, Bull. Acad. Sci. USSR, Math. Ser. **1**, 355 (1937).

[38] W. A. Johnson and R. F. Mehl, Reaction kinetics in processes of nucleation and growth, Trans. AIME **135**, 416 (1939).

[39] M. Avrami, Kinetics of phase change. I. General theory, J. Chem. Phys. **7**, 1103 (1939); Kinetics of phase change. II. Transformation time relations for random distribution of nuclei, J. Chem. Phys. **8**, 212 (1940); Granulation, phase change and microstructure kinetics of phase change. III, J. Chem. Phys. **9**, 177 (1941).

[40] C. Ratsch, Strain dependence for microscopic growth parameters for Ag on Ag(100), Phys. Rev. B **83**, 153406 (2011).

[41] L. Huang, F. Liu, G.-H. Lu, and X. G. Gong, Surface Mobility Difference between Si and Ge and Its Effect on Growth of SiGe Alloy Films and Islands, Phys. Rev. Lett. **96**, 016103 (2006).